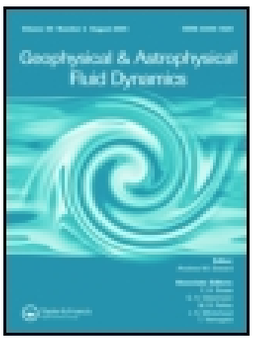

Taylor & Francis
Taylor & Francis Group

Geophysical & Astrophysical Fluid Dynamics

ISSN: 0309-1929 (Print) 1029-0419 (Online) Journal homepage: https://www.tandfonline.com/loi/ggaf20

Testing Alfvén wave propagation in a "realistic" set-up of the solar atmosphere

Piyali Chatterjee

To cite this article: Piyali Chatterjee (2019): Testing Alfvén wave propagation in a "realistic" set-up of the solar atmosphere, Geophysical & Astrophysical Fluid Dynamics, DOI: 10.1080/03091929.2019.1672676

To link to this article: https://doi.org/10.1080/03091929.2019.1672676

Published online: 25 Oct 2019.

GEOPHYSICAL & ASTROPHYSICAL FLUID DYNAMICS
https://doi.org/10.1080/03091929.2019.1672676

Taylor & Francis
Taylor & Francis Group

Testing Alfvén wave propagation in a "realistic" set-up of the solar atmosphere

Piyali Chatterjee

Indian Institute of Astrophysics, Bengaluru, India

ABSTRACT

We present a radiative magneto-hydrodynamic simulation set-up using the pencil code to study the generation, propagation and dissipation of Alfvén waves in the solar atmosphere which includes a convective layer, photosphere below and chromosphere, transition region and the corona above. We prepare a set-up of steady-state solar convection where the imposed external magnetic field also has reached the final value gradually starting from a very small value. From that state, we start several simulations by varying the magnetic Prandtl number and the forcing strengths. We find the propagation characteristics of waves excited in this simulation run depend strongly on the magnetic Prandtl number and the wave number of the forcing. For magnetic Prandtl number of unity, we obtain localised heating in the corona due to shock dissipation.

ARTICLE HISTORY
Received 20 June 2018
Accepted 23 September 2019

KEYWORDS
Magneto-hydrodynamics; Alfvén waves; solar-atmosphere

1. Introduction

The reason for a hot solar corona still remains a grand challenge problem in the field of plasma physics. The observation of highly ionised Iron in the solar corona requires evenly high temperatures to maintain these ionisation equilibria (Grotrian 1934). A high degree of ionisation of several elements in the corona also points to high temperatures (Edlén 1943). A canonical value of a million Kelvin (MK) usually quoted for coronal plasma temperatures certainly cannot be the black body radiation temperature as the plasma is tenuous and optically thin. It may represent the kinetic electron temperature, T_e – which has been measured using line ratios of coronal emission lines like Si XII/Mg X, Si XII/Mg IX, or Mg X/Mg IX observed with the CDS instrument on SOHO and assuming that the plasma is isothermal and has a Maxwellian velocity distribution giving values like 1.6 MK in coronal streamers and 0.8 MK in polar coronal holes (Fludra *et al.* 1999) or from radio emission due to free-free thermal Bremsstrahlung around optically thick 170 MHz emission giving temperatures of about 0.64 MK (Fokker 1966). It may also be the ion temperature (T_i) measured using the line widths of emission lines and can be significantly hotter than T_e (Landi and Cranmer 2009) or the proton temperature (T_p) the upper limit of which could be ∼6 MK, obtained from the HI Ly α line widths in polar coronal holes (Kohl *et al.* 1998; Vásquez *et al.* 2003). Also, both T_i and T_p are said to be highly anisotropic depending

CONTACT Piyali Chatterjee piyali.chatterjee@iiap.res.in

on if the measurement is parallel or perpendicular to the radial magnetic field. Therefore, it is not clear to us what the temperature, T used in the magneto hydrodynamic (MHD) approximation for the coronal plasma (described with a single fluid density, ρ) should correspond to out of T_e, T_p and T_i. Nevertheless, the problem remains to devise one or several mechanisms to accelerate the electrons, protons and ions in the plasma to high enough energies to be able to explain the emission line ratios, the line widths and the radio emission from the solar corona. Two competing theories acknowledged by experts are the wave heating or AC models and the DC models which include nanoflares (Parker 1981, 1983), heating along separatrix layers in the corona due to *flux tube tectonics* (Priest *et al.* 2002) and slow diffusive (Bourdin *et al.* 2013) and fast intermittent reconnections (Bingert and Peter 2011, 2013). Many early authors introduced the idea that Alfvén wave steepening and dissipation in the solar atmosphere may be a candidate for the million Kelvin corona (Alfvén 1947; Ferraro and Plumpton 1958; Osterbrock 1961). Alfvén or shear Alfvén waves are incompressible normal modes of magneto hydrodynamic equations characterized by transverse motion of magnetic field lines. A peculiar property of these incompressible waves is that they are exact solutions of the full non-linear MHD equations irrespective of their amplitudes and thus can travel long distances into the heliosphere before depositing their energy as compared to compressive modes (Ofman 2002). The other solutions of MHD equations – slow magneto acoustic mode will decay before even reaching the corona and can at most contribute to heating the upper chromosphere, the fast magneto acoustic mode will likely undergo refractions in a highly stratified atmosphere before reaching the corona. Solar chromosphere is believed to be a vast reservoir of wave energy – compressible or incompressible modes – that has been observed (Morton *et al.* 2012) using the ROSA imager for the Dunn solar telescope. Even though incompressible Alfvén waves can travel far into the corona without refraction, these modes are very difficult to dissipate under solar atmospheric conditions and require large Alfvén speed gradients or presence of highly non-uniform magnetic fields like flux tubes. Observationally Alfvén waves have also been observed in coronal holes and in the fast solar wind as observed by the Helios and Ulysses missions (Marsch 1991; Goldstein *et al.* 1995). It is therefore possible that Alfvén wave heating takes place in coronal holes at heights above where the fast solar wind originates. We believe that in the lower corona, or in the quiet sun and above active regions, the Ohmic heating due to magnetic reconnection can compete with Alfvén wave dissipation. Some authors, using numerical MHD models, but extending only up to ≤ 37 Mm above the photosphere, report that Parker's nanoflare model is sufficient to heat the corona to million degree Kelvin (Gudiksen and Nordlund 2002, 2005; Bingert and Peter 2011, 2013). These state-of-the-art three-dimensional Cartesian models are also referred to as "realistic" because of their treatment of the magnetic field-aligned thermal conduction, radiative transfer assuming local thermodynamic equilibrium or LTE (Bingert and Peter 2011; Bourdin *et al.* 2013; Chen *et al.* 2014; Rempel 2017) or the treatment of partial ionisation and non-LTE effects in the chromosphere (Gudiksen *et al.* 2011). Recently, Ryu and Huynh (2017) have used the Flash code as well as the Pencil code (Brandenburg and Dobler 2002) to study Alfvén wave dissipation in a two-dimensional solar atmosphere between 1 Mm $< z <$ 10 Mm for a simulation duration of $\sim$500 s solar time. Khomenko and Cally (2011) have also used a 2.5D MHD model up to 1 Mm height to study the conversion of fast magneto acoustic modes to Alfvén modes in the chromosphere in the presence of an inclined magnetic field of strength 500 G. van Ballegooijen *et al.* (2017) used

a 3D MHD extending up to a height of 50 Mm but with reduced physics to study AC heating in the form of Alfvén wave turbulence and showed that it is sufficient to heat coronal loops to MK temperatures. But, to the best of our knowledge, the two models of heating (AC and DC) have never been compared using the same numerical code and under similar thermodynamic conditions. This work has been initiated with the aim of building such models in 2D, 2.5D and 3D where the contribution from the MHD shock waves, Alfvén wave dissipation, reconnection and nano flare heating can be studied. In the present work, we would like to clarify that whenever we use term "realistic", we refer to the vertical stratification of the atmosphere as well as to the fact that we use field-aligned anisotropic thermal conduction and (LTE) radiative transfer. The convection developing in our 2D model is far from the real Sun since 3D Rayleigh–Bénard hexagonal convection cells are fundamentally different from the 2D convection rolls. Also, the direction of energy cascade in wavenumber space is opposite in 2D and 3D. Previous authors (Bingert and Peter 2011, 2013; Bourdin *et al.* 2013) have already used the pencil code to model a "realistic" solar corona. For example, see the sample set up – `solar-atmosphere-magnetic` – for a set-up spanning $-2.6\,\mathrm{Mm} < z < 0.6\,\mathrm{Mm}$, where $z = 0$ denotes the position of the photosphere and, another sample set-up – `corona` – spanning $0 < z < 40$ Mm. In the latter set up the solar atmosphere is driven at the lower boundary by a granulation driver which mimics the solar photospheric convection and a magnetogram driver which provides a time-varying vertical magnetic field at the photosphere. The reader is also referred to the manual which comes with the pencil code distribution for further details of the equations. In this paper, we present the creation of a "realistic" but two-dimensional solar atmosphere including subsurface convection, photosphere, chromosphere and a corona as well as for the first time incorporate the semi-relativistic Boris correction into the Pencil code. Boris correction, which is a way of reducing numerical diffusion and the need for using large explicit diffusion in MHD simulations, solves the semi-relativistic magnetohydrodynamics equations with an artificially reduced speed of light. This correction was introduced by Boris (1970) and later incorporated in MHD codes like BATS-R-US (Gombosi *et al.* 2002) and, MuRAM (Rempel 2017). An alternate fully implicit time-stepping scheme – Implicit Scheme with Limited Numerical Dissipation (ISLND) – was developed and benchmarked with Boris correction by Tóth *et al.* (2011) with comparable results. We also use a specific form of the hyperbolic heat transport equation into the pencil code. We then test our model set up for the propagation and dissipation of MHD waves in the presence of an external oblique magnetic field.

2. Setting up the pencil code for the solar atmosphere

The computational domain consists of a box, the horizontal extents of which are $-6.25\,\mathrm{Mm} < x < 6.25\,\mathrm{Mm}$, and the vertical extent is $-10\,\mathrm{Mm} < z < 15.0\,\mathrm{Mm}$. A constant gravity, g_z, with magnitude $-2.74 \times 10^4\,\mathrm{cm\,s^{-2}}$ points in the negative z-direction. The $z = 0$ height denotes the solar photosphere and the region between $-10\,\mathrm{Mm} < z < 0$ represents uppermost part of the solar convection zone. The box is resolved using a uniformly spaced grid with $\mathrm{d}z, \mathrm{d}x = 48$ km. We use the fully compressible higher-order finite difference tool, the Pencil Code[1] for these calculations. We use a sixth-order finite

[1] https://github.com/pencil-code/

difference scheme and a second-order Runge–Kutta time-stepping scheme out of several other options available with the pencil code. This code is highly modular and can easily be adapted to different types of computational MHD problems. We solve the following set of compressible MHD equations. The continuity equation is given by

$$\frac{\mathrm{D}\ln\rho}{\mathrm{D}t} = -\boldsymbol{\nabla}\cdot\boldsymbol{U}, \tag{1}$$

where $\mathrm{D}/\mathrm{D}t \equiv \partial/\partial t + \boldsymbol{U}\cdot\boldsymbol{\nabla}$ denotes the Lagrangian derivative with respect to the local velocity of the gas, $\boldsymbol{U}$, and ρ is the local plasma density in units of the photospheric density, $\rho_0 = 2.7 \times 10^{-7}\,\mathrm{g\,cm^{-3}}$.

Equation of state: We use an equation of state which includes ionisation calculated assuming local thermal equilibrium(LTE). The pressure, p, is given by

$$p = \frac{\rho R_g T}{\mu(T)},$$

where $R_g = k_B/m_u$ is the ideal gas constant, T is the temperature and μ is the effective mass given by

$$\mu = \frac{4x_{\mathrm{He}} + 1}{y_{\mathrm{H}}(T) + x_{\mathrm{He}} + 1}.$$

We consider the number fraction of Helium, x_{He}, to have a constant value of 0.089, whereas the fraction of ionised Hydrogen, denoted by y_{H} is a function of temperature. To calculate, $y_{\mathrm{H}}(T)$, at each time step, using the Saha's ionisation formula. We solve the following quadratic equation in y_{H} (Bhat and Brandenburg 2016):

$$\frac{y_{\mathrm{H}}^2}{1 - y_{\mathrm{H}}} = q \tag{2}$$

with the equilibrium reaction constant

$$q = \frac{\rho_{\mathrm{e}}}{\rho}\left(\frac{\chi_{\mathrm{H}}}{k_B T}\right)^{-3/2} \exp(-\chi_H/k_B T),$$

and whose solution is given by

$$y_{\mathrm{H}} = \frac{2\sqrt{q}}{\sqrt{q} + \sqrt{4+q}} \tag{3}$$

with

$$\rho_e = (1 + 4x_{\mathrm{He}})m_u\left(\frac{m_e\chi_{\mathrm{H}}}{2\pi\hbar^2}\right)^{3/2}.$$

Here, $\chi_{\mathrm{H}} = 13.6\,\mathrm{eV}$, m_u is 1 amu and, m_e, the mass of electron. The momentum equation is

$$\frac{\mathrm{D}\boldsymbol{U}}{\mathrm{D}t} = -\frac{\boldsymbol{\nabla}p}{\rho} + g_z\hat{\boldsymbol{z}} + \frac{\boldsymbol{J}\times\boldsymbol{B}}{\rho} + \boldsymbol{F}_L^{\mathrm{corr}} + \rho^{-1}\mathbf{F}_{\mathrm{visc}}, \tag{4}$$

where $\boldsymbol{J}$ is the current density, $\boldsymbol{B}$ is the magnetic field, $\boldsymbol{F}_L^{\mathrm{corr}}$ is the semi-relativistic correction due to Boris (1970) which has been discussed in Section 2.1. The viscous force is

modelled as

$$\rho^{-1}\mathbf{F}_{\rm visc} = \nu\left(\nabla^2\boldsymbol{U} + \tfrac{1}{3}\boldsymbol{\nabla}\boldsymbol{\nabla}\cdot\boldsymbol{U} + 2\mathbf{S}\cdot\boldsymbol{\nabla}\ln\rho\right) + \zeta_{\rm shock}\left[\boldsymbol{\nabla}\left(\boldsymbol{\nabla}\cdot\boldsymbol{U}\right) + \left(\boldsymbol{\nabla}\ln\rho + \boldsymbol{\nabla}\ln\zeta_{\rm shock}\right)\boldsymbol{\nabla}\cdot\boldsymbol{U}\right], \tag{5}$$

where ν is the height-dependent kinematic viscosity, and $\mathbf{S}$ is the traceless rate-of-strain tensor. We also use an enhanced viscous force at the shock fronts. The expression for the coefficient $\zeta_{\rm shock}$ in (5) is given by

$$\zeta_{\rm shock} = \nu_{\rm shock}\left\langle {\rm Max}_3\left[(-\boldsymbol{\nabla}\cdot\boldsymbol{U})_+\right]\right\rangle, \tag{6}$$

where $\langle {\rm Max}_3[(-\boldsymbol{\nabla}\cdot\boldsymbol{U})_+]\rangle$ means that to each grid point, we assign a value given by the maximum of the positive flow convergence ($-\boldsymbol{\nabla}\cdot\boldsymbol{U} > 0$) over three neighbouring grid points along each spatial dimension and then smooth the result using a running mean over three neighbouring grid points along each coordinate direction. The induction equation is solved for the magnetic vector potential, $\boldsymbol{A}$, using the uncurled induction equation

$$\frac{\partial\boldsymbol{A}}{\partial t} = \boldsymbol{U}\times\boldsymbol{B} - \eta\mu_0\boldsymbol{J} + \boldsymbol{\nabla}\Psi. \tag{7}$$

In the presence of an external magnetic field, $\boldsymbol{B}_{\rm ext}$, $\boldsymbol{B} = \boldsymbol{B}_{\rm ext} + \boldsymbol{B}'$ and $\boldsymbol{\nabla}\times\boldsymbol{A} = \boldsymbol{B}'$ and η denotes molecular magnetic diffusivity. Gauge freedom allows us to set $\Psi = 0$ (Weyl gauge) at all times.

The initial stratification of temperature is obtained by collating the Model S Christensen-Dalsgaard *et al.* (1996) for the interior and the atmospheric model by Vernazza *et al.* (1981). The initial density stratification corresponding to this temperature is obtained by solving the hydrostatic balance subjected to the ionised ideal gas equation of state with ionisation fraction given by the Saha-ionisation formula (see (3)).

Finally, we have for the temperature equation, with turbulent diffusion, χ_t,

$$\rho c_V T\frac{{\rm D}\ln T}{{\rm D}t} = -(\gamma-1)\rho c_v T\boldsymbol{\nabla}\cdot\boldsymbol{U} + \boldsymbol{\nabla}\cdot(\boldsymbol{q}_{\rm cond} + \boldsymbol{q}_{\rm rad}) + \boldsymbol{\nabla}\cdot(\rho T\chi_t\boldsymbol{\nabla}\ln T) + \eta\mu_0\boldsymbol{J}^2 + 2\rho\nu\mathsf{S}_{ij}^2 + \rho\zeta_{\rm shock}\left(\boldsymbol{\nabla}\cdot\boldsymbol{U}\right)^2 - \rho^2\Lambda(T). \tag{8}$$

The Spitzer heat conduction flux is denoted $\boldsymbol{q}_{\rm cond}$ and described in Section 2.2, S_{ij}^2 denote the square of the tensorial components of the rate-of-strain tensor, $\mathbf{S}$ summed over all indices, *i*,*j* and, c_V is the specific heat capacity at constant volume.

Radiative transport: The radiative flux is denoted by $\boldsymbol{q}_{\rm rad}$ and is calculated using the method of long characteristics as described in Heinemann *et al.* (2006). To compute $\boldsymbol{\nabla}\cdot\boldsymbol{q}_{\rm rad}$, we solve the equation of radiative transport by adopting a grey approximation, and by neglecting scattering contributions

$$\hat{\boldsymbol{n}}\cdot\boldsymbol{\nabla}I = -\kappa_{\rm tot}\rho(I-S), \tag{9}$$

where $I(x,z,t,\hat{\boldsymbol{n}})$ is the specific intensity along direction $\hat{\boldsymbol{n}}$. The source function $S = (\sigma_{\rm SB}/\pi)T^4$ is the frequency integrated Planck's function with $\sigma_{\rm SB}$ being the

Stefan–Boltzman constant. The integration of (9) over solid angle, Ω, will give us $\boldsymbol{\nabla}\cdot\boldsymbol{q}_{\rm rad}$ by

$$\boldsymbol{\nabla}\cdot\boldsymbol{q}_{\rm rad} = \kappa_{\rm tot}\rho \oint_{4\pi} (I - S)\, {\rm d}\Omega. \tag{10}$$

For this angular quadrature we use eight rays, 4 along x and z axes and 4 along face diagonals of the x–z grid, and correctly scale the angular weight factors for two dimensionality (Barekat and Brandenburg 2014). We do not use tabulated opacities, rather use analytical power-law fits to Rosseland mean opacity functions. We use solar abundances $X = 0.7381$, $Y = 0.2485$, metallicity $Z = 0.0134$. The bound-free, free-free and H^- opacities are combined to give the total opacity, $\kappa_{\rm tot}$. The Rosseland mean of the bound-free and free-free opacities can be written in the Kramers power-law form (Hansen and Kawaler 1994)

$$\kappa_{\rm bf+ff} \sim 4 \times 10^{25} Z(X+1)\rho T^{-7/2}\ {\rm cm^2 g^{-1}},$$

whereas the H^- opacity which cannot be expressed in a Kramers power-law form is given by

$$\kappa_{\rm H^-} \sim 1.25 \times 10^{-29} Z\rho^{1/2} T^9\ {\rm cm^2 g^{-1}}.$$

The conductive opacity due to the electron scattering, for partial ionisation is

$$\kappa_{\rm c} = 2.6 \times 10^{-7} \frac{T^2}{\rho}\ {\rm cm^2 g^{-1}}.$$

The total opacity is then given by

$$\frac{1}{\kappa_{\rm tot}} = \frac{1}{\kappa_r} + \frac{1}{\kappa_c} \quad \text{where } \frac{1}{\kappa_r} = \frac{1}{\kappa_{\rm bf+ff}} + \frac{1}{\kappa_{\rm H^-}}.$$

Following the MuRAM code (Rempel 2017) where the radiative module is shut off once transition region is reached, we smoothly put the source function, S and the opacity, $\kappa_{\rm tot}$, to zero above $z = z_{\rm cutoff} = 1.5$ Mm to avoid contribution from the transition region and corona in the downward directed rays. For a high temperature in the corona, the Planck source function used in the radiative transfer equation will have a huge value and therefore is not realistic. Hence we do not take such back reaction into account. Additionally, in order to limit the numerical value of radiative heating, we use an upper bound 10^3 ergs cm^{-3} s^{-1} for $\boldsymbol{\nabla}\cdot\boldsymbol{q}_{\rm rad}$ before adding it to (8). The transport of radiation through chromosphere normally gives rise to cooling ($\boldsymbol{\nabla}\cdot\boldsymbol{q}_{\rm rad} < 0$) rather than heating ($\boldsymbol{\nabla}\cdot\boldsymbol{q}_{\rm rad} > 0$) since some of the solar energy passing through the chromosphere is absorbed by atoms to make transitions to higher energy states (or even get ionised) and therefore is not available for raising the temperature of the chromospheric plasma. The situation is highly dynamic during first few mins (solar time) of the simulation run when shocks are passing repeatedly through this region. After 1 hour of solar time, when the convection has settled to a steady state, changing the upper limit to a much higher positive value does not affect the simulation. In fact, $q_{\rm rad}$ does not exceed 25% of its maximum negative value in the domain. The last term in (8) is the optically thin radiative cooling which is activated in the solar corona only for $z > z_{\rm cutoff}$ and is obtained by best fits to Cook *et al.* (1989) by using a linear piecewise interpolation algorithm in log T. This corresponds to setting the parameter `cool_type=5` in the `solar_corona` special module in the Pencil code.

Table 1. Summary of the runs.

	R_0	R_1	R_2	R_3
f	4×10^5	4×10^5	4×10^3	4×10^4
η_0 (cm^2 s^{-1})	10^8	10^8	2×10^{11}	8×10^{12}
Pr_M	8×10^5	8×10^5	4	1
$k_x L_x/2\pi$	1	1	1	8
u_y^{ff} (km s^{-1})	1	5	5	2

Notes: The parameters are defined in the text. The run R_0 is the original run described in detail whereas the runs, R_1, R_2 and R_3 and branched from a particular snapshot of R_0 at different times.

Boundary conditions and explicit dissipation: The lower boundary at $z_B = -10$ Mm is forced by a sinusoidal velocity forcing with an amplitude $u_f = (L_\odot/4\pi\rho(z_B)R_\odot^2)^{1/3}$ and the top boundary at $z_T = 15.0$ Mm is open. The solar luminosity and radius are denoted by symbols $L_\odot$ and $R_\odot$, respectively. The purpose of the lower boundary driving is to excite waves of particular horizontal wavenumber comparable to the granulation scale. It also helps development of convection faster than cases where we do not include this driving. The density and temperature are considered to be in hydrostatic balance at either vertical boundary. This means that the slopes, $\mathrm{d}\ln\rho/\mathrm{d}z$ and $\mathrm{d}\ln T/\mathrm{d}z$, in the ghost zones are set to values expected from hydrostatic balance at the vertical boundaries. The x-boundaries are periodic. Our simulation set-up is different from that presented in Rempel (2017) in the way that we have not used opacity tables and a tabulated equation of state. Analytical expressions for the opacity approximating the tabulated opacity tables and the Saha ionisation formula has been used. The treatment of the top boundary is also different in that in Rempel (2017), a sponge-like top boundary is used for the fluid velocity in contrast to here where we put the vertical derivatives of U_x and U_y to zero and we also set $\mathrm{d}U_z/\mathrm{d}z = 0$ only if we detect an outflow, else if we detect any plasma inflow at any horizontal grid point at the top boundary, we set $U_z = 0$, and for the magnetic field, we replicate the value of the electromotive force, $\mathcal{E} = -\boldsymbol{U} \times \boldsymbol{B}$ of the last grid point to all ghost cells. Our top boundary allows reflection of the MHD waves in spite of allowing matter and energy to flow out since we do not solve for the equation of characteristics at the boundary for MHD waves. For specific intensity, we assume zero intensity at the top and set it equal to the source function at the bottom. We include explicit height-dependent viscosity, $\nu/\nu_0 = 1 + f[1 + \tanh((z - z_1)/w)]$, with, $f = 4 \times 10^5, z_1 = 1$ Mm, $w = 1.5$ Mm, $\nu_0 = 10^8$ cm^2 s^{-1}, whereas for the magnetic diffusivity, we use a uniform and constant value of $\eta_0 = 10^8$ cm^2 s^{-1} unless specified (see table 1). The turbulent diffusion, $\chi_t = 10^8$ cm^2 s^{-1} for $z < 0$ and goes to zero above that. Additionally, we use hyper-diffusion and up-winding to reign in the high frequency wiggles. A density diffusion of 4×10^8 cm^2 s^{-1} is also included for numerical stability.

2.1. Semirelativistic Boris correction to Lorentz force

In earlier works, MHD simulations have used Lorentz force limiters of the form $(1 + v_A^2/c_s^2)^{-1}$ as a multiplying factor for the Lorentz force for low plasma β atmospheres. However, Moradi and Cally (2013) found that these traditional limiters reduce the outward Poynting flux of MHD waves considerably. Instead they explore an alternative method of empirically modifying the density and the gravity from a solar-like atmosphere which in

turn modifies the acoustic cut-off frequency above the surface. The need for having a semi-relativistic correction to the Lorentz force term in the velocity equation (4) comes from the fact that in non-relativistic plasmas, the Alfvén velocity, $v_A = B/\sqrt{\mu_0 \rho}$ can become comparable to the speed of light, c. For example, in the solar corona above the active regions, the magnetic field can be as large as 190 G inside coronal flux rope (Chatterjee and Fan 2013) with a plasma density of $\sim 1.8 \times 10^{-17}$ g cm^{-3}, $v_A/c = 0.42$. At these speeds of wave propagation, the plasma can no longer be non-relativistic and we cannot neglect the displacement current in the induction equation. While the treatment of electrodynamics is relativistic, the velocity equation remains non-relativistic, making this a semi-relativistic correction. Boris (1970) found that by retaining the displacement current, the wave speeds are upper bounded by the speed of light. In order to accelerate the convergence of the explicitly numerical schemes by taking larger time strides, he proposed artificially lowering the c. The Pencil Code solves for the non-conservative form of the velocity equation, because of which, we follow the primitive variable formulation of the semi-relativistic correction from Gombosi *et al.* (2002). Here, the velocity equation is modified in the following way:

$$\left[\mathbf{I} + \frac{v_A^2}{c^2}\left(\mathbf{I} - \hat{\boldsymbol{b}}\hat{\boldsymbol{b}}\right)\right] \cdot \frac{\partial \boldsymbol{U}}{\partial t} = -(\boldsymbol{U}\cdot\boldsymbol{\nabla})\boldsymbol{U} - \frac{\boldsymbol{\nabla} p}{\rho} + g_z \hat{\boldsymbol{z}} + \left[\frac{(\boldsymbol{\nabla} \times \boldsymbol{B})}{\mu_0 \rho} + \frac{(\boldsymbol{\nabla} \times \boldsymbol{E}) \times \boldsymbol{U}}{\mu_0 \rho c^2}\right] \times \boldsymbol{B}. \tag{11}$$

The term multiplying the $\partial \boldsymbol{U}/\partial t$ on the left-hand side of (11) can be thought of as an "enhanced inertia" matrix (Rempel 2017) which makes motion perpendicular to the magnetic field increasingly difficult while the motion parallel to the field lines remains purely hydrodynamic. The limit of validity of the semi-relativistic correction is $|\boldsymbol{U}| \ll c < v_A$. We follow Rempel (2017) and use $c^2 = \max(c_s^2, 25|\boldsymbol{U}|^2_{\max})$ as the artificially limited speed of light, with c_s denoting the speed of sound. However, we do not let c fall below a value of $c_{\min} = 300$ km s^{-1} above the photosphere, whereas in the convective layer c still has the value 3×10^{10} cm s^{-1}. For the value of $c_{\min}$ used, we find that the local Alfvén speed $> c_{\min}$ at about 8000 grid points out of a total of 131072 grid points. These grid points typically located at the top of the box, where the plasma density is lowest, are where the Boris correction applies strongly. Now, let us consider the relative importance of the last two terms (inside square brackets) in (11):

$$\frac{|(\boldsymbol{\nabla} \times \boldsymbol{E}) \times \boldsymbol{U}|}{c^2 |\boldsymbol{\nabla} \times \boldsymbol{B}|} \sim \frac{|\boldsymbol{U}|^2}{c^2} \ll 1. \tag{12}$$

It follows that the last term in (11) consisting of the Electric field, $\boldsymbol{E}$, can be neglected. Note that the viscosity terms have not been modified while implementing the Boris correction. Now, the inverse of the "enhanced inertia" term, after denoting $\beta_A^2 = v_A^2/c^2$, can be approximated as

$$\left[\mathbf{I} + \beta_A^2\left(\mathbf{I} - \hat{\boldsymbol{b}}\hat{\boldsymbol{b}}\right)\right]^{-1} = \frac{1}{1+\beta_A^2}\left[\mathbf{I} + \frac{\beta_A^2}{1+\beta_A^2}\hat{\boldsymbol{b}}\hat{\boldsymbol{b}}\right] = \mathbf{I} - \frac{\beta_A^2}{1+\beta_A^2}\left[\mathbf{I} - \frac{\hat{\boldsymbol{b}}\hat{\boldsymbol{b}}}{1+\beta_A^2}\right]. \tag{13}$$

It is worth noting that the expression of the inverted "enhanced inertia" matrix in (13) is more accurate than equation (52) of Rempel (2017). With this approximation the

correction to the forces on the right-hand side of (4) is given by

$$F_L^{\rm corr} = \frac{\beta_A^2}{1+\beta_A^2}\left[\mathbf{I} - \frac{\hat{\boldsymbol{b}}\hat{\boldsymbol{b}}}{1+\beta_A^2}\right]\left[\boldsymbol{U}\cdot\boldsymbol{\nabla}\boldsymbol{U} + \frac{\boldsymbol{\nabla}p}{\rho} - g_z\hat{\boldsymbol{z}} - \frac{(\boldsymbol{\nabla}\times\boldsymbol{B})\times\boldsymbol{B}}{\mu_0\rho}\right]. \tag{14}$$

In the pencil code, the Boris semi-relativistic correction can be switched on by setting the flag `lboris_correction=T` in the name list `magnetic_run_pars` in the file ?extttrun.in. According to Gombosi *et al.* (2002), the characteristic speeds due to the Boris correction are modified in a non-trivial manner which is expected to relax the time step constraint due to the fastest wave mode. The time step calculation has been modified in the code by replacing the Alfvén speed, v_A with $v_A/(1+v_A^2/c^2)^{1/2}$ in the calculation of the Courant criteria. In runs R_0–R_2, where the magnetic field is only 5 G, the time step is governed mainly by the time step imposed by the `radiation_ray` module in the code. However, when we increase the magnetic field strength to 50 G, thereby increasing the Alfvén speed, we find that the time step imposed by the `radiation_ray` and `magnetic` modules are comparable. For such large Alfvén speeds ($\sim$7000 km s^{-1}), the Boris correction also allows our code to be numerically stable for long simulation times when we set $c_{\rm min} = 3000\,{\rm km\,s^{-1}}$. The formulation of the Boris correction in the Pencil code has also been used by Warnecke and Bingert (2019) for a 3D simulation set-up of the solar corona.

2.2. The hyperbolic heat transport equation

The anisotropic thermal conduction along magnetic field lines increases to very large values at the high temperatures of the solar corona, constraining the time step severely if the conductivity is treated using explicit numerical schemes. Some methods for circumventing this difficulty include either treating the conduction term implicitly or by using a time sub-stepping scheme. The time sub-stepping scheme is also available for use in the pencil code but we have not tested that for this work. The hyperbolic diffusion equation also known as non-Fickian transport equation has been used earlier by several authors in the dynamo community: in the context non-locality of the mean field electromotive force using the telegraph equation approach (Brandenburg *et al.* 2004; Hubbard and Brandenburg 2009; Rheinhardt and Brandenburg 2012; Brandenburg and Chatterjee 2018). Such schemes have also been used by Rempel (2017) and Fan (2017) for treating the anisotropic Spitzer conductivity in the solar corona – the same purpose as here. This formulation to treat the Spitzer heat conduction is available in the `heatflux` module of the pencil code. There are three different formulations available again by different authors. Here, we have used the formulation using the subroutine `nonadvective_nonfourier_spitzer`. Let $q_{\rm cond}$ denote the solution of the non-Fickian transport equation like (15) and $q_{\rm sp}$ denote the expression of the conduction flux according to the Spitzer model. It follows that

$$\frac{\partial \boldsymbol{q}_{\rm cond}}{\partial t} = -\frac{\boldsymbol{q}_{\rm cond} - \boldsymbol{q}_{\rm sp}}{\tau_{\rm sp}} + \beta(\mathrm{d}\boldsymbol{r}\cdot\boldsymbol{\nabla})^6\boldsymbol{q}_{\rm cond}, \tag{15}$$

where

$$\boldsymbol{q}_{\rm sp} = K_{\rm sp}T^{5/2}\hat{\boldsymbol{b}}(\hat{\boldsymbol{b}}\cdot\boldsymbol{\nabla}T),$$

and whenever,

$$\chi_{\rm sp} = \frac{K_{\rm sp} T^{5/2}}{\rho c_V} > f_{sp} c_0 \delta x,$$

we set the Spitzer diffusion coefficient, $\chi_{\rm sp}$ to a fraction $f_{\rm sp}$ of the electron free streaming limit $c_0 \delta x$. Here, c_0 is the actual speed of light, δx is the maximum grid size and, the Spitzer coefficient, $K_{\rm sp}$, has a value 10^{-6} erg cm^{-1} s^{-1} K$^{-7/2}$ and, $\hat{\boldsymbol{b}}$ is the unit vector in the direction of the magnetic field including the externally imposed one. We take a small value for the fraction, $f_{sp} = 0.1$, $\tau_{\rm sp} = 0.1$ s, and the numerical hyper diffusion term, defined using $\mathrm{d}\boldsymbol{r} = (\mathrm{d}x, \mathrm{d}y, \mathrm{d}z)$ and with $\beta = 100\,\mathrm{s}^{-1}$ suppresses numerical wiggles. Compared to the explicit time stepping, we gain a factor of ∼100 on the time step by using this method. Our time step varies between 0.6−10 ms.

A sample run directory available as part of the Pencil code distribution is located at `samples/2d-tests/SolarAtmosMag+Boris_Corr+Heatflux` and contains the start (run) parameters in the files `start.in (run.in)`, the initial stratification file, and a reference output file. We encourage users interested in this simulation to start from this run directory. Additionally, the compilation files `src/Makefile.local` provides the list of physics modules used, and `src/cparam.local` sets the grid size as well as the number of cpus used in each coordinate direction.

3. Results: Alfvén waves in the simulation

We start our simulation with the density and temperature stratification shown in figure 1(a) but with a Gaussian noise with a half width of $\sigma = 0.1$ km s^{-1} for the velocity components. For the first 10 min of solar time, while the initial atmosphere is adjusting to the physics in the simulation, we use a velocity damping in the corona. Due to the super-adiabatic unstable stratification between $-10\,\mathrm{Mm} < z < 0$, the convection gradually sets in and the convective energy $\langle \rho U^2 \rangle$ reaches a steady value by $t = 68$ min. The resultant stratification at $t = 68$ min and a snapshot of the vertical velocity is shown in the panels (a) and (b) of figure 1. Note that in this figure as the time in the simulation increases, the temperature in the corona part of the domain decreases due to the optically thin cooling profiles used and in absence of any explicit heating function. This cooling causes the density in the corona to also increase. This will be a challenge for any heating source trying to re-heat the collapsing, be it wave dissipation or reconnection, as it has more coronal material to heat in order to increase the temperature. The residual magnetic field in the simulation atmosphere is very weak and we do not expect the dynamics to be affected due to magnetic reconnection. The external field, which is not acted upon by the flow, is oriented in the $\hat{\boldsymbol{x}} + \hat{\boldsymbol{z}}$ direction and is increased from 0.1 to 5.0 G gradually within a duration of 75 min of solar time. After this $B_{\rm ext}$ is kept fixed at 5.0 G. This gradual increase of $B_{\rm ext}$ is necessary since this prevents the numerical value of density from reducing to very low values during the adjustment of the initial atmosphere to the included physics. During this time the maximum Alfvén speed in the domain increases from 210 to 770 km s^{-1}. The $B_{\rm ext}$ inclined at an angle $\theta = 45^\circ$ to the vertical is used to facilitate the conversion of fast magneto-acoustic modes to Alfvén modes as suggested by Cally and Goossens (2008) as well as Cally and Hansen (2011) where they found that the conversion efficiency depends sensitively on angles θ and the azimuth, ϕ at which the fast waves are incident on the external magnetic field. In our case $\phi = 0$ for

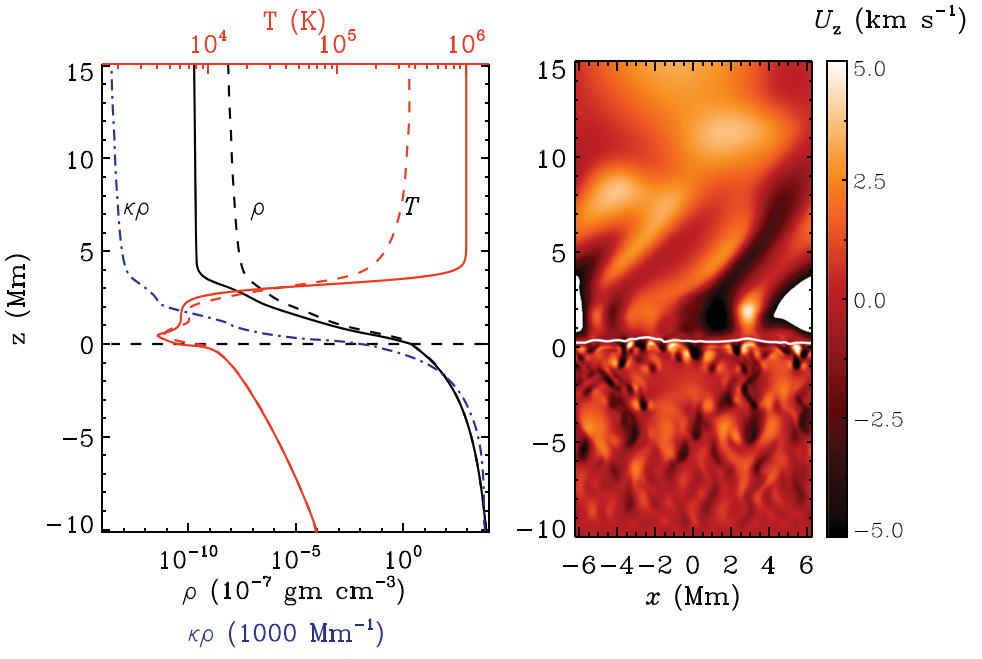

Figure 1. (a) Vertical profiles of the initial (solid) and steady state (dashed) convective temperature (red) and density (black) in the domain. The blue dashed-dotted line shows the profile of $\kappa\rho$ after steady state of convection has been reached. (b) The vertical velocity in the x–z plane at $t = 68$ min after the start of the simulation. The white curve shows the location of the optical depth, $\tau = 1$ "surface" (colour online).

convective motions and $\phi = 90^\circ$ for the motion excited due to the forcing $\mathcal{F}_y$ described below, where as Cally and Hansen (2011) find that $\phi \sim 60^\circ$–90° and $\theta \sim 30^\circ$–40° leads to near total conversion of fast mode to Alfvén waves and is completely absent for $\theta = 0$ or for purely vertical magnetic fields.

Since this is a 2.5 -dimensional set-up, we expect all the MHD modes – slow and fast magnetoacoustic waves, linearly and circularly polarised Alfvén waves can be excited in the simulation. As the magnetic field in the domain is homogenous, we do not expect surface modes like torsional or sausage modes in this simulation. These surface modes constitute another vast field of study and have also been detected in the upper solar chromosphere (Jess *et al.* 2009) using data from the Swedish Solar Telescope. However, here our aim is to only study the propagation and damping properties of shear Alfvén waves excited due to the convection and in the context of the semi relativistic Boris correction implemented here. We find that the amplitude of U_y is quite less ($\sim$0.1 km s^{-1}) because of the 2.5-dimensional rather than full 3-dimensional set-up. We separate the velocity vector into components in normal, $\hat{\boldsymbol{n}} = (\hat{\boldsymbol{z}} - \hat{\boldsymbol{x}})/\sqrt{2}$ and tangential, $\hat{\boldsymbol{t}} = (\hat{\boldsymbol{z}} + \hat{\boldsymbol{x}})/\sqrt{2}$ directions with reference to the external magnetic field which points towards $\hat{\boldsymbol{t}}$. So, in order to drive a linearly polarised Alfvén wave with perturbations in the $\hat{\boldsymbol{y}}$ direction, we force the system between $0.6 < z < 1$ Mm with a forcing $\mathcal{F}_y \sim u_y^{ff} \sin(k_x x + k_z z - \omega t)/\omega$ in the y-component of the velocity equation. Note that the driving is only in terms of the perturbed velocity and not the magnetic field $\boldsymbol{B}'$. We expect that the induction equation will produce a perturbed magnetic field corresponding to this velocity driving. We consider the time

period of the driving to be $2\pi/\omega = 100\,\mathrm{s}$ and amplitude $u_y^{ff} = 1\,\mathrm{km\,s^{-1}}$. Note that this driving introduced in the interior of the box is different from that at the bottom boundary. We additionally require this internal driving as the strength of the velocity driving at the bottom boundary by itself is unable to generate enough power in the variability of the y-component of the velocity. However, we start this driving only for $t > 83$ min after the start of the simulation, long after the external magnetic field has reached its final value of 5.0 G. For now, the external magnetic field is taken to be uniform in contrast to that expected in the solar atmosphere where the magnetic field would exist in flux tubes or loops. The top boundary does reflect some of the MHD waves as we have not imposed the characteristic equations for the magneto-acoustic and Alfvén waves at the top. But, this is alright as wave reflection is a common phenomena in the line-tied magnetic loops in the atmosphere. The snapshots of the three different components of the velocity – U_y, U_n, and U_t – at a time $t = 100.5$ min for run, R_0, is shown in figure 2. Panel (a) of this figure shows propagation of positive and negative U_y phases along the direction of the external guide field. The snapshot in panels (b) have clear signatures of modes that are reflected where as, panel (c) which shows U_t shows patterns aligned in the $\boldsymbol{t}$ direction. From the animation corresponding to this figure, we clearly see waves propagating in the $+x$ direction. The snapshots of the perturbation $\boldsymbol{v}'_A$ in figure 3 is more complex. For example, the contours of constant phase are mis-aligned with the external magnetic field. For Alfvén waves, we expect $\boldsymbol{U}$ and $\boldsymbol{v}'_A$ to have equal amplitudes so as to satisfy equipartition of energy between magnetic field and the velocity. This seems not to be the case here. The likely reasons for this is the large magnetic

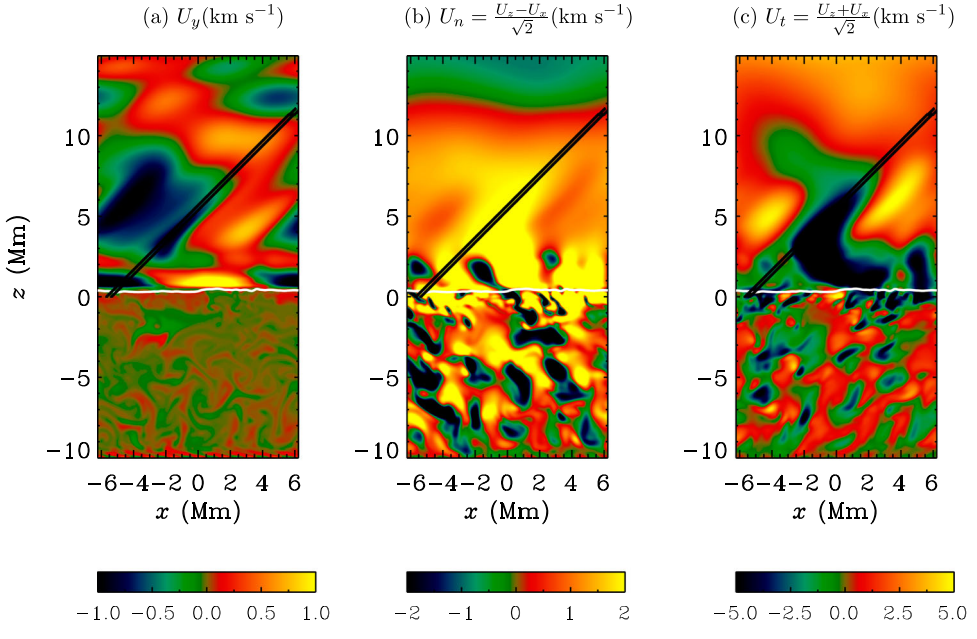

Figure 2. Snapshots of velocity components in $\hat{\boldsymbol{y}}$, $\hat{\boldsymbol{n}}$ and, $\hat{\boldsymbol{t}}$ directions at a time $t = 100.5$ min after the start of the simulation run, R_0. The black slanted lines denote the location of the slit (along the $\hat{\boldsymbol{t}}$-direction) while the white curve is the optical depth, $\tau = 1$ surface. This figure is available as an animation (colour online).

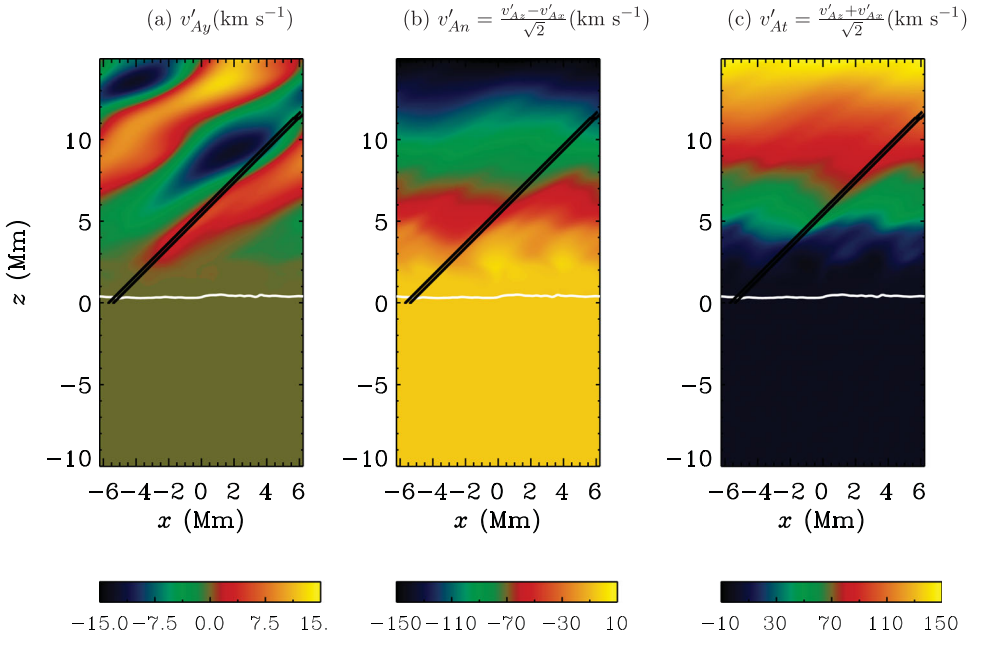

Figure 3. Snapshots of components of Alfvén velocity, v'_A, in $\hat{\boldsymbol{y}}$, $\hat{\boldsymbol{n}}$ and, $\hat{\boldsymbol{t}}$ directions at a time $t = 100$ min after the start of the simulation for run R_0. The black slanted lines denote the location of the slit (along the $\hat{\boldsymbol{t}}$-direction) and the white curve is the optical depth, $\tau = 1$ surface. This figure is available as an animation (colour online).

Prandtl number ($Pr_M = \nu/\eta \gg 1$) as well as modification of the structure of the modes due to the semi relativistic correction. We present time evolution diagrams for the velocity and magnetic field components in figures 4 and 5 along a slit shown by the black line in figures 2 and 3 aligned along the $\hat{\boldsymbol{t}}$-direction (same as the direction of the externally applied magnetic field). The slit width over which the pattern has been averaged is 0.3 Mm. In panel (a) of figures 4 and 5, the amplitudes of U_y and v'_{Ay} are substantial and has a time period of 1.67 min only after $t = 83$ min which is a clear signature of the driving $\mathcal{F}_y$. In both figures 4 and 5, the first thing we notice is that the time-period for U_y and v'_{Ay} (1.67 min from panel a) is less than that of other components in the $\hat{\boldsymbol{n}}$ and $\hat{\boldsymbol{t}}$ directions (4.8 min and 5.5 respectively in panels b and c). The time periods have been calculated from the inspection of the waveforms in regions where the amplitudes are stronger, e.g. at $s = 4$ Mm for components U_y and U_t and at $s = 12$ Mm for the component U_n. For $t < 100$ min, we have only forced the velocity in the y-direction, exciting a linearly polarised Alfvén wave mode. Also, the presence of non-zero velocity component in the $\hat{\boldsymbol{t}}$ direction (along $\boldsymbol{B}_{\rm ext}$) implies excitation of magneto-acoustic waves, as Alfvén waves are transverse and cannot have a velocity component in the direction of the external guide field. In fact, this component, U_t, has a consistent amplitude throughout the simulation duration and is not affected by the forcing (in the y-direction) switched on for $t > 83$ min and is a result of the two-dimensional convection. The average speeds of propagation is fastest for U_n in panel (b) and slowest for U_t in panel (c) of figure 4.

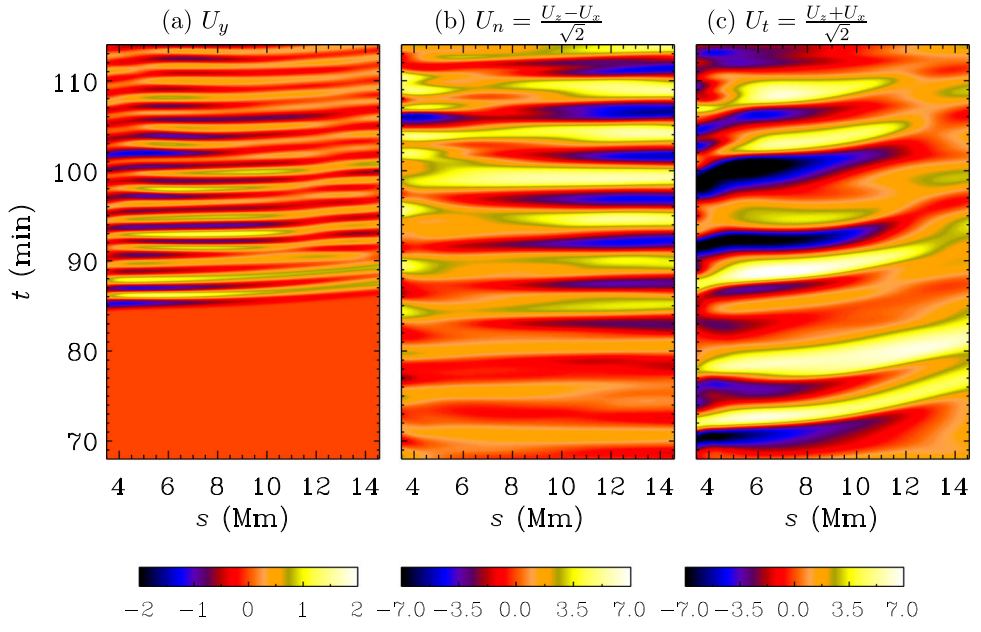

Figure 4. The time-distance maps for run R_0 corresponding to the simulation duration between $70 < t < 112$ min averaged over the width of the slit shown in the panels of figure 2 for (a) U_y, (b) U_n and (c) U_t. The abscissa is the length along the slit and the velocity components are in units of km s^{-1} (colour online).

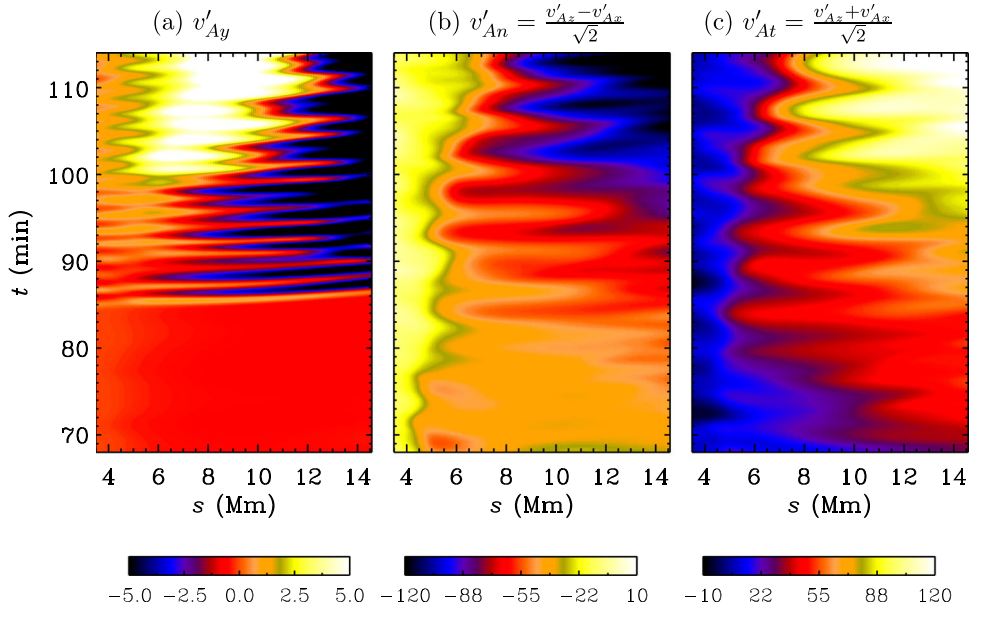

Figure 5. The time-distance maps for the run R_0 corresponding to the simulation duration between $70 < t < 112$ min averaged over the width of the slit shown in the panels of figure 2 for (a) v'_{Ay}, (b) v'_{An} and (c) v'_{At}. The abscissa is the length along the slit and the velocity components are in units of km s^{-1} (colour online).

We show the z-component of the horizontally averaged Poynting flux, $\boldsymbol{S}$, only due to the waves in figure 6. We calculate this flux using

$$S = \frac{1}{L_x}\int \frac{\boldsymbol{B}' \times (\boldsymbol{U} \times \boldsymbol{B})}{\mu_0}\,\mathrm{d}x.$$

The vertical component S_z shows an increase of amplitude when the velocity forcing is switched on. The dominant time period as clear from panel (a) is 4.8 min which is the same periodicity as seen in U_n in figure 4(b). The alternating sign of negative and positive Poynting flux is a signature of modes interfering due to reflection. If the wave energy existed only as transverse waves, for which $\boldsymbol{B}'\cdot\boldsymbol{B} = 0$, the Poynting flux term will be $\propto -\rho(\boldsymbol{v}'_A\cdot\boldsymbol{U})\boldsymbol{v}_A$. A better way to estimate the contribution of the transverse Alfvén waves to S_z would be to estimate $-\langle\rho(\boldsymbol{v}'_{A\perp}\cdot\boldsymbol{U}_\perp)v_{Az}\rangle$, where $\langle\rangle$ denotes horizontal averaging and, with $\boldsymbol{v}'_{A\perp} = v'_{An}\hat{\boldsymbol{n}} + v'_{Ay}\hat{\boldsymbol{y}}$ (see panel b of figure 6). Clearly, the transverse waves have a major contribution to the spatio-temporal pattern of S_z. In panel (c) of figure 6, we show the net Poynting flux injected in the region 4 Mm $< z <$ 13.9 Mm by the simple formula $\Delta S_z = S_{z1} - S_{z2}$ (solid black line). When $\Delta S_z > 0$ for extended time intervals, excess energy is available for heating the corona, where as for $\Delta S_z < 0$ also for extended time intervals, the corona between z_1 and z_2 will cool during this time interval. The running average of ΔS_z over a time interval 2.5 min is shown in red. We see that average of

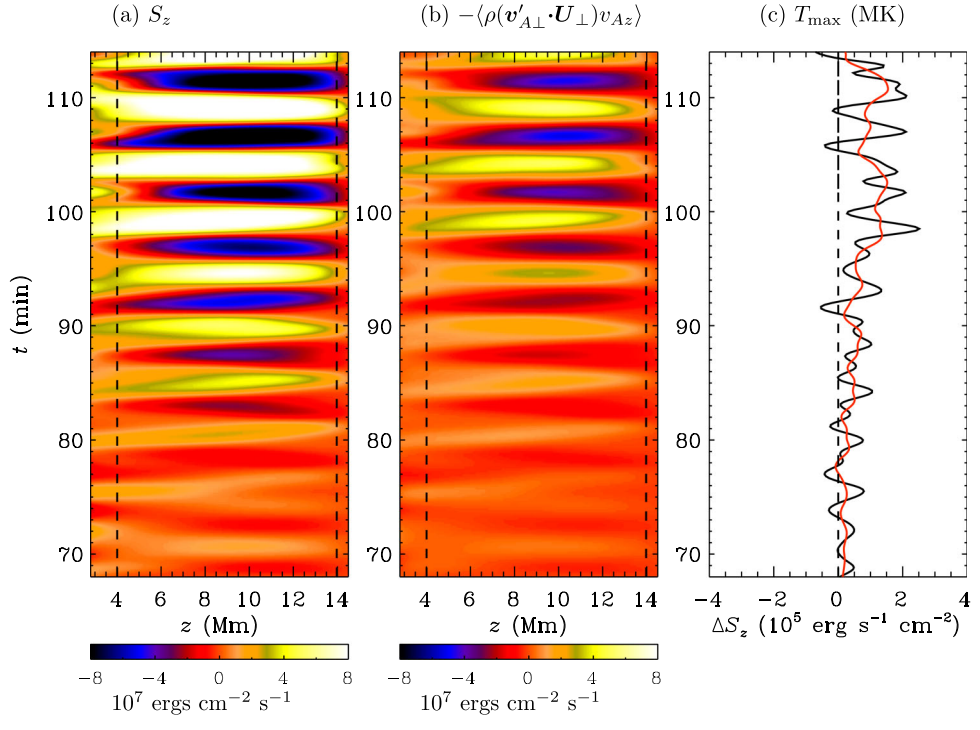

Figure 6. (a) The vertical component of the horizontally averaged Poynting flux as a function of time for R_0. The time period ∼5 min. (b) The contribution to the vertical Poynting flux from transverse waves. (c) $\Delta S_z = S_{z1} - S_{z2}$ (black), calculated by taking $z_1 = 4$ Mm and $z_2 = 13.9$ Mm denoted by dashed lines in panel (a). The red curve is the running mean calculated with a time interval 2.5 min (colour online).

ΔS_z can reach values of 10^5 ergs cm^{-2} s^{-1} in the lower solar corona below 15 Mm. This value can be compared with a Poynting flux of 5×10^7 ergs s^{-1} cm^{-2} produced by the photospheric driver corresponding to an active region (without any well-formed sunspot pair observed by the SOT instrument on board the Hinode satellite on 14 Nov 2007) used in a 3D MHD model for coronal loops (Bourdin *et al.* 2014, 2015). We also performed an alternate run R_1, branching from the original run R_0 presented above at $t = 98$ min, where we only increased the amplitude, u_y^{ff}, of the forcing, $\mathcal{F}_y$, by a factor of five. Now, these waves cannot be classified as small amplitude waves anymore. Interestingly, we found that in this run, the amplitude U_y is often a factor of about 10 smaller than $-v'_{Ay}$ (see figure 7) at $t = 103.8$ min. As we have mentioned earlier that in the semi relativistic limit the Alfvén speeds are quite different from the classical MHD case and that may explain the factor of 10 difference in the fluid velocity and Alfvén velocity perturbations. However, the patterns of U_y and v'_{Ay} again diverged after $t = 110$ min. This may have happened due to the very large explicit magnetic Prandtl number chosen in the corona part of the simulation, inspired by the expression for viscosity and resistivity given by Spitzer (1962). We tested this hypothesis successfully by reducing $Pr_M \sim 4$ (i.e. by reducing $f = 10^3$) in yet another run R_2 where $u_y^{ff} = 0.5$ and branched from the run R_0 at $t = 83$ min and the patterns of U_y and v'_{Ay} continued to be in anti-phase for 20 min after the restart from R_0. For run R_2, the amplitude U_y is again a factor of ten smaller than $-v'_{Ay}$. From panels (a) and (b) of this figure we can infer that the plane of polarisation of these propagating waves lies in a direction given by $\boldsymbol{k} \times \boldsymbol{B}_{\rm ext}$ (or in the $\hat{\boldsymbol{y}}$ direction), where $\boldsymbol{k}$ is the wave vector and makes an angle $\sim 15^\circ$ with the guide field, $\boldsymbol{B}_{\rm ext}$. Also we can see that the magnitude of the wave vector is $\sim 2\pi/Lx$. The dispersion relation for incompressible Alfvén waves in a homogenous atmosphere without stratification can be easily obtained by linearising the MHD equations (4) and (7) (without the Boris correction term) and is given by

$$\omega^2 + \mathrm{i}(\nu + \eta)k^2\omega - \nu\eta k^4 - v_A^2 k^2 = 0. \tag{16}$$

This is a very simple relation and is not correct for our present simulation set-up. Nevertheless, the imaginary part of the solution of this quadratic equation is given by $\mathrm{i}(\nu + \eta)k^2/2$. An approximate estimate for decay time of Alfvén waves in our simulation using the above equation is $\sim$33 min which will lead to a very slow heat rate by wave dissipation. One way of reducing this decay time will be to use a large wavenumber in the x-direction for the driving $\mathcal{F}_y$ (Ryu and Huynh 2017). We also test this by increasing the horizontal wave number in the run, R_3. From the dispersion relation (16). the real part of the frequency has the form $\sqrt{v_A^2 k^2 - (\nu - \eta)^2 k^4}/2$. For large Pr_M, there would be a region in the corona where Alfvén waves (for small Alfvén velocities and large k like here) will be evanescent. However, for $Pr_M = 1$ this problem does not arise. Therefore, in the run R_3, we also change the Prandtl number to be one. Besides, we also change the height for the forcing to lie between 2 Mm $< z <$ 2.2 Mm, so that the forcing frequency ω can take a value of $v_A k \sim 0.02\pi$ rad s^{-1}. The waves produced by the driving in R_3 propagate in a direction more aligned to the field $\boldsymbol{B}_{\rm ext}$ (not shown) in comparison to the run R_0 (see figures 2(a) and 7(a)). We started this run from an early snapshot of run R_0 at $t = 76.3$ min. The decay time for the $kL_x/2\pi = 8$ is expected to be 0.05 min from the simple equation (16). Nevertheless, we see that the maximum temperature in the domain (during the simulation duration of 53 min of solar time after introduction of the forcing at $t = 76.3$ min) increases

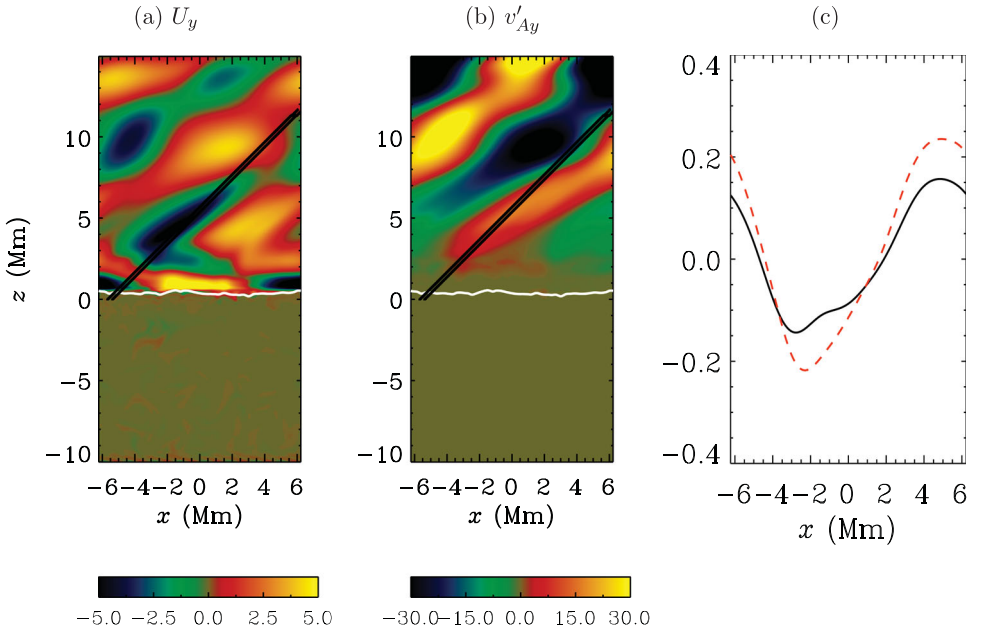

Figure 7. (a) A snapshot of U_y in the domain at $t = 103.8$ min for the run R_1 with the forcing enhanced after $t > 98$ min. (b) A snapshot of v'_{Ay} at the same time. (c) Horizontal profiles of U_y (solid) and $-v'_{Ay}/10$ (dashed) at $z = 12$ Mm (colour online).

and fluctuates between $2 \times 10^5 < T < 1.2 \times 10^6$ presumably due to Alfvén wave dissipation as opposed to the run R_0 (panel (c) of figure 8). It is worth noting that for all the other runs, the temperature in the corona part of the domain decreases with time logarithmically rather than exponentially as seen in the panel (c) of figure 8 (solid black line). Note that, the forcing u_y^{ff} was not switched on at the time when the runs – R_1, R_2 and R_3 – branched from R_0. It is possible that shock fronts appearing in the simulation run, R_3, as a result of branching from run, R_0, by means of change of parameters like the Prandtl number has caused these localised temperature enhancements. But, this is unlikely as we found episodes where the maximum temperature exceeded 1 MK in a run with same parameters like R_3 but initiated at $t = 0$ from same initial conditions as R_0 instead of branching from it. In this test run, after the episodic bursts of high temperature, the maximum temperature eventually decayed like the other runs, R_0, R_1 and R_2. Because of the above reasons, we do not claim this heating as a consistent feature arising out of Alfvén wave dissipation. The Poynting flux is larger in magnitude in the run R_3 as compared to the run R_0 as shown in figure 8(a). Until $t = 120$ min, the time-distance diagram of the vertical Poynting flux show similar slopes for positive and negative phases in both figures 6(a) and 8(a) but, after this the speed of propagation seems to decrease for the run R_3. This may be because the propagation direction becomes more horizontal and the effective vertical speed decreases as evident from animation of the snapshots of U_y, U_n and, U_t in the domain available as an animation file: run3.mp4 in accompanying supplementary material. In the animation the white arrows denote the direction (not magnitude) of the total magnetic field including $\boldsymbol{B}_{\rm ext}$. We should also note that in run $R3$, the waves excited may be finite amplitude waves

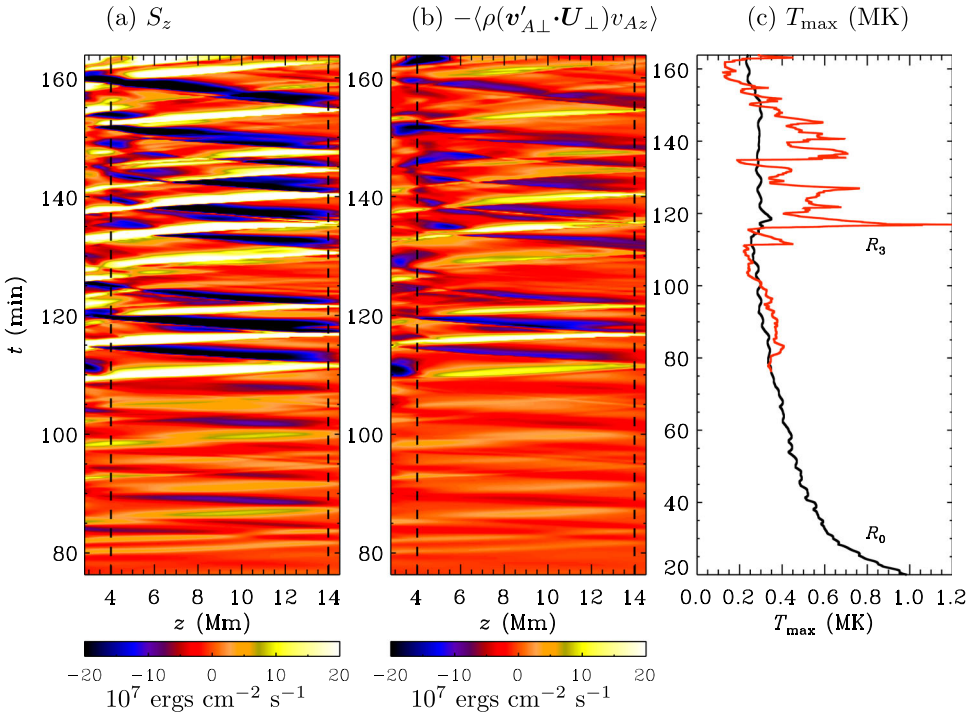

Figure 8. (a) The vertical component of the horizontally averaged Poynting flux as a function of time for R_3. (b) The contribution to the vertical Poynting flux from transverse waves. (c) The time-evolution of the maximum temperature in the domain for the two runs R_0 (black solid) and R_3 (red) (colour online).

which can modify the guide magnetic field from the given $\boldsymbol{B}_{\rm ext}$. In the panel (b) of the same figure, we show the contribution of the transverse waves to the Poynting flux, namely, $\langle-\rho(\boldsymbol{v}'_{A\perp}\cdot\boldsymbol{U}_\perp)\boldsymbol{v}_A\rangle$. Here also like in figure 6(b), the transverse waves majorly contribute to the spatio-temporal pattern of S_z.

4. Discussion

We present a 2.5-dimensional Cartesian radiative MHD set-up using the pencil code in a first step towards understanding the propagation of Alfvén waves in an atmosphere with a "realistic" solar-like stratification. We incorporated the semi relativistic Boris correction in the velocity equation for numerical stability and also use a hyperbolic heat transport equation to bypass the time-stepping constraint due to an explicit field-aligned thermal conduction. We consider spatial variations only in the x–z plane with z as the direction of stratification. The velocity and the magnetic field has components in the y-direction but has no variation with the y axis. The lower part of the box is convective below $z < 0$, but being 2.5-dimensional the amplitude of U_y is much smaller than U_x and U_z. Hence, in order to excite Alfvén waves, we drive the system with an artificial forcing, $\mathcal{F}_y$, in the y-component of the velocity equation with a frequency 100 Hz and an amplitude such that the mean U_y between 0.6 Mm $< z <$ 1 Mm is $\sim$0.7 km s^{-1}. This value is still a factor of five smaller than the other velocity components in the x–z plane. The forcing $\mathcal{F}_y$ can excite linearly polarised

Alfvén waves with the plane of polarisation perpendicular to the vector $\hat{\boldsymbol{n}}$ which can propagate out of the domain with a group velocity $\boldsymbol{v}_A$. This is evident from the fact that the time taken to traverse a distance of 10 Mm along the slit is ∼1 min from figure 4(a) and matches with the estimate obtained by integrating $\int \mathrm{d}s/v_A(s)$ between $4\,\mathrm{Mm} < z < 14\,\mathrm{Mm}$, where $\mathrm{d}s$ is the infinitesimal element along the slit and $v_A(s)$ is the Alfvén speed along the external guide field. We believe that the mismatch in the spatial and temporal patterns of fluid velocity and the perturbation magnetic field, $\boldsymbol{B}'$ in the run R_0 is due to a very large value of the Prandtl number used in the coronal part of the simulation. The runs here have been continued for about 110 min of solar time during which the dynamics have been influenced by the magnetic Prandtl number as well as the nature of the forcing employed. For all runs reported in table 1 except R_3, the temperature in the corona decreases logarithmically. For R_3, we see some heating in the form of local enhancements of temperature which is intermittent in time but still decreases during the end of the simulation run. The external magnetic field used in this set-up is not the correct reproduction of the magnetic field topologies in the Sun where Alfvén velocities will be large in the chromosphere and transition region coronal loops. So far, we have tested and found the set-up to be stable for maximum Alfvén speeds reaching as large as $4.04\,\mathrm{Mm\,s^{-1}}$. In the future simulations, we wish to explore external magnetic field resembling coronal loop-like geometries and strengths rather than a simple inclined uniform and weak magnetic field used here. The driving we have used here is located much above the photosphere. With coronal loop like external magnetic fields, we can circumvent the need of this artificial driving at ∼2 Mm as the driving velocities will be channelled to the corona along the strong magnetic loops from underneath the photosphere much faster. In this 2.5-dimensional set-up, however, we cannot do away with the forcing $\mathcal{F}_y$ completely since $|U_y| < |U_{x,z}|$, but, the forcing can then be set up underneath the photosphere rather than above it. It is also important to explore the role of reconnection which we have neglected here and compare with the contributions of wave heating. These are the topics of future explorations using the Pencil code set-up described here.

Acknowledgments

We thank the two anonymous referees for carefully reviewing the manuscript which has lead to considerable improvement upon its clarity. We acknowledge the computing time awarded on PARAM Yuva-II supercomputer at C-DAC, India under the grant name Hydromagnetic-Turbulence-PR. Most of the simulation runs were carried out on the HPC cluster, Nova, of the Indian Institute of Astrophysics. We thank P.A. Bourdin and Jörn Warnecke for discussions on the code especially related to the solar corona module. We also thank Sahel Dey, for his project work on dispersion relations of Alfvén waves.

Disclosure statement

No potential conflict of interest was reported by the author.

ORCID

Piyali Chatterjee http://orcid.org/0000-0002-0181-2495

References

Alfvén, H., Magneto hydrodynamic waves, and the heating of the solar corona. *Mon. Not. R. Astron. Soc.* 1947, **107**, 211–213.

Barekat, A and Brandenburg, A., Near-polytropic stellar simulations with a radiative surface. *Astron. Astrophys.* 2014, **571**, A68–A84.

Bhat, P. and Brandenburg, A., Hydraulic effects in a radiative atmosphere with ionization. *Astron. Astrophys.* 2016, **587**, A90–A102.

Bingert, S. and Peter, H., Intermittent heating in the solar corona employing a 3D MHD model. *Astron. Astrophys.* 2011, **530**, 112–124.

Bingert, S. and Peter, H., Nanoflare statistics in an active region 3D MHD coronal model. *Astron. Astrophys.* 2013, **550**, 30–38.

Boris, J.P, A physically motivated solution of the Alfvén problem, Navel Research Laboratory Memorandum Report, Vol. 2167, 1970.

Bourdin, Ph.-A., Bingert, S. and Peter, H., Observationally driven 3D magnetohydrodynamics model of the solar corona above an active region. *Astron. Astrophys.* 2013, **555**, 123–129.

Bourdin, Ph.-A., Bingert, S. and Peter, H., Coronal loops above an active region: Observation versus model. *Publ. Astron. Soc. Jpn.* 2014, **66**, S7–15.

Bourdin, Ph.-A., Bingert, S. and Peter, H., Coronal energy input and dissipation in a solar active region 3D MHD model. *Astron. Astrophys.* 2015, **580**, A72–80.

Brandenburg, A. and Chatterjee, P., Strong nonlocality variations in a spherical mean-field dynamo. *Astron. Nachrich.* 2018, **339**, 118–126.

Brandenburg, A. and Dobler, W., Hydromagnetic turbulence in computer simulations. *Comput. Phys. Commun.* 2002, **147**, 471–475.

Brandenburg, A., Käpylä, P.J. and Mohammed, A., Non-Fickian diffusion and tau approximation from numerical turbulence. *Phys. Fluids* 2004, **16**, 1020–1027.

Cally, P.S. and Goossens, M., Three-dimensional MHD wave propagation and conversion to Alfvén waves near the solar surface. I. Direct numerical solution. *Solar Phys.* 2008, **251**, 251–265.

Cally, P.S. and Hansen, S.C., Benchmarking fast-to-Alfvén mode conversion in a cold magnetohydrodynamic plasma. *Astrophys. J.* 2011, **738**, 119–131.

Chatterjee, P. and Fan, Y., Simulation of homologous and cannibalistic coronal mass ejections produced by the emergence of a twisted flux rope into the solar corona. *Astrophys. J.* 2013, **778**, L8–L13.

Chen, F., Peter, H., Bingert, S. and Cheung, M.C.M., A model for the formation of the active region corona driven by magnetic flux emergence. *Astron. Astrophys.* 2014, **564**, 12–25.

Christensen-Dalsgaard, J., Dappen, W., Ajukov, S.V., Anderson, E.R., Antia, H.M. and Basu, S., *et al.* The current state of solar modeling. *Science* 1996, **272**, 1286–1292.

Cook, J.W., Cheng, C.-C., Jacobs, V.L. and Antiochos, S.K., Effect of coronal elemental abundances on the radiative loss function. *Astrophys. J.* 1989, **338**, 1176–1183.

Edlén, B., Die Deutung der Emissionslinien im Spektrum der Sonnenkorona. Mit 6 Abbildungen. *Zeit. für Ap.* 1943, **22**, 30–64.

Fan, Y., MHD simulations of the eruption of coronal flux ropes under coronal streamers. *Astrophys. J.* 2017, **844**, 26–45.

Ferraro, C.A. and Plumpton, C., Hydromagnetic waves in a horizontally stratified atmosphere. *Astrophys. J.* 1958, **127**, 459–476.

Fludra, A., Del Zanna, G., Alexander, D. and Bromage, B.J.I., Electron density and temperature of the lower solar corona. *J. Geophys. Res.* 1999, **104**, 9709–9720.

Fokker, A.D., The electron temperature of the solar corona as derived from radio observations. *Bull. Astron. Inst. Netherlands* 1966, **18**, 359.

Goldstein, M.L., Roberts, D.A. and Matthaeus, W.H., Magnetohydrodynamic turbulence in the solar wind. *Annu. Rev. Astron. Astrophys.* 1995, **33**, 283–326.

Gombosi, T.I., Tóth, G., De Zeeuw, D.L., Hansen, K.C., Kabin, K. and Powell, K.G., Semirelativistic magnetohydrodynamics and physics-based convergence acceleration. *J. Comput. Phys.* 2002, **177**, 176–205.
Grotrian, W., Über das Fraunhofersche spektrum der sonnenkorona. Mit 10 Abbildungen. *Zeit. für Ap.* 1934, **8**, 124–146.
Gudiksen, B.V. and Nordlund, Å., Bulk heating and slender magnetic loops in the solar corona. *Astrophys. J.* 2002, **572**, L113–L117.
Gudiksen, B.V. and Nordlund, Å., An ab initio approach to the solar coronal heating problem. *Astrophys. J.* 2005, **618**, 1020–1030.
Gudiksen, B.V., Carlsson, M., FokHansteenker, V.H., Hayek, W., Leenaarts, J., and Martí-nez-Sykora, J., The stellar atmosphere simulation code Bifrost. *Code description and validation, A & A* 2011, **531**, 19.
Hansen, C.J. and Kawaler, S.D., *Stellar Interiors: Physical Principles, Structure, and Evolution*, 1994 (Springer-Verlag: New York).
Heinemann, T., Dobler, W., Nordlund, Å. and Brandenburg, A., Radiative transfer in decomposed domains. *Astron. Astrophys.* 2006, **448**, 731–737.
Hubbard, A. and Brandenburg, A., Memory effects in turbulent transport. *Astrophys. J.* 2009, **706**, 712–726.
Jess, D.B., Mathioudakis, M., Erdélyi, R., Crockett, P.J., Keenan, F.P. and Christian, D.J., Alfvén waves in the lower solar atmosphere. *Science* 2009, **323**, 1582–1585.
Khomenko, E. and Cally, P.S., Numerical simulations of conversion to Alfvén waves in solar active regions. *J. Phys.: Conf. Ser.* 2011, **271**, 012042.
Kohl, J.L., Noci, G., Antonucci, E., Tondello, G., Huber, M.C.E. and Cranmer, S.R., *et al.* UVCS/SOHO empirical determinations of anisotropic velocity distributions in the solar corona. *Astrophys. J.* 1998, **501**, L127–L131.
Landi, E. and Cranmer, S.R., Ion temperatures in the low solar corona: Polar coronal holes at solar minimum. *Astrophys. J.* 2009, **691**, 794–805.
Marsch, E., MHD Turbulence in the Solar Wind. In *Physics of the Inner Heliosphere, Vol. 2: Particles, Waves and Turbulence*, edited by R. Schwenn, E. Marsch, vol. 20, pp. 159–241, 1991 (Berlin: Springer).
Moradi, H. and Cally, P.S., Modelling fast-Alfvén mode conversion using SPARC. *J. Phys.: Conf. Ser.* 2013, **440**, 012047.
Morton, R.J., Verth, G., Jess, D.B., Kuridze, D., Ruderman, M.S., Mathioudakis, M. and Erdélyi, R., Observations of ubiquitous compressive waves in the Sun's chromosphere. *Nat. Commun.* 2012, **3**, 1315.
Ofman, L., Chromospheric leakage of Alfvé. *Astrophys. J.* 2002, **568**, L135–L138.
Osterbrock, D.E., The heating of the solar chromosphere, plages, and corona by magnetohydrodynamic waves. *Astrophys. J.* 1961, **134**, 347–388.
Parker, E.N., The dissipation of inhomogeneous magnetic fields and the problem of coronae – part two – the dynamics of dislocated flux. *Astrophys. J.* 1981, **244**, 644–652.
Parker, E.N., Magnetic neutral sheets in evolving fields – part two – formation of the solar corona. *Astrophys. J.* 1983, **264**, 642–647.
Priest, E.R., Heyvaerts, J.F. and Title, A.M., A flux-tube tectonics model for solar coronal heating driven by the magnetic carpet. *Astrophys. J.* 2002, **576**, 533–551.
Rempel, M., Extension of the MURaM radiative MHD code for coronal simulations. *Astrophys. J.* 2017, **834**, 10–33.
Rheinhardt, M. and Brandenburg, A., Modeling spatio-temporal nonlocality in mean-field dynamos. *Astron. Nachrich.* 2012, **333**, 71–77.
Ryu, Chang-Mo and Huynh, C.T., Propagation and damping of Alfvén waves in low solar atmosphere. *Mon. Not. R. Astron. Soc.* 2017, **471**, 2237–2241.
Tóth, G., Meng, X., Gombosi, T.I. and Ridley, Aaron J., Reducing numerical diffusion in magnetospheric simulations. *J. Geophys. Res.* 2011, **116**, A07211.
van Ballegooijen, A.A., Asgari-Targhi, M. and Voss, A., The heating of solar coronal loops by Alfvé. *Astrophys. J.* 2017, **849**, 46–69.

Vásquez, A.M., van Ballegooijen, A.A. and Raymond, J.C., The effect of proton temperature anisotropy on the solar minimum corona and wind. *Astrophys. J.* 2003, **598**, 1361–1374.
Vernazza, J.E., Avrett, E.H. and Loeser, R., Structure of the solar chromosphere. III – Models of the EUV brightness components of the quiet-sun. *Astrophys. J. Supp. Ser.* 1981, **45**, 635–725.
Warnecke, J. and Bingert, S, Non-Fourier description of heat flux evolution in 3D MHD simulations of the solar corona. arXiv:1811.01572, 2019.